Journal of Hazardous Materials Advances 12 (2023) 100368

Contents lists available at ScienceDirect

Journal of Hazardous Materials Advances

journal homepage: www.elsevier.com/locate/hazadv

Ultrasonic radiation assisted synthesis of $(CH_3NH_3)_2CuCl_4$, $CH_3NH_3PbCl_3$, and $CH_3NH_3SnCl_3$ perovskites for energy application

Swapna Shambulinga Chigari [a], Vidyasagar C. C [a,*], Vishwanath C. C [b,*], Sanakousar Faniband M [a], Vinay Kumar B [c], Raghu A. V [d]

[a] Department of Chemistry, Rani Channamma University, Belgaum 591156, India
[b] Department of Chemistry, J.S.S. Arts, Science & Commerce College, Gokak 591307, India
[c] Department of Chemistry, RNS Institute of Technology, Uttarahalli-Kengeri Main Road, Channasandra, Bengaluru 560098 Karnataka, India
[d] Faculty of Science and Technology, BLDE (Deemed to be University), Vijayapura 586103 Karnataka, India

ARTICLE INFO

Keywords:
Band gap
Electrical
Lead-free
Optical
Perovskites

ABSTRACT

The present research provides an outline for the synthesis of organic-inorganic hybrid perovskites such as $(CH_3NH_3)_2CuCl_4$, $CH_3NH_3PbCl_3$, and $CH_3NH_3SnCl_3$ by using Ultrasonic radiation assisted method. An X-ray diffraction study reveals the presence of crystalline phase in the Cu, Pb and Sn based perovskites. The optical and electrical properties were carefully examined using UV–Vis diffuse reflectance spectroscopy. The optical band gaps of the synthesized sample were estimated using Tauc's plot. The current-voltage characteristics of all the samples demonstrate increase in photocurrent under UV light compared to darkness. The findings indicated that the addressed samples are improved in the visible absorption region and were in good agreement with earlier research. The photo-induced mechanisms that result in the remarkable charge separation efficiency of these materials are fundamental properties that provide insight into the special features of such a material which has driven this to the forefront of photovoltaic research.

1. Introduction

Perovskite has acquired much attention in recent years and has made remarkable advances in energy storage, contaminant degradation, and optoelectronics because of its superior optoelectronic and catalytic properties, that have allowed it come forefront (Noel et al., 2014). Perovskite compounds, which might be classified into inorganic perovskite and organic-inorganic hybrid perovskite, are all materials with an ABX_3 structure (Dey et al., 2021). Crystal structure of ABX_3 perovskites (A=organic cation, B=divalent metal cation, X=halide) include BX_3 octahedral cations surrounded by the methyl ammonium cation (A) (C. C. Vidyasagar et al., 2018) Recently both inorganic and organic-inorganic hybrid perovskites have been reported to have advantages in energy application, but hybrid perovskites are frequently regarded as being preferable for their tunable optoelectronic properties, high absorption coefficients (Li et al., 2021), long carrier diffusion length (Kumavat et al., 2019), defect tolerance etc. (Haug et al., 2014). Miyasaka et al. reported the first usage of organo-metal halide perovskites in solar cells in 2009 (Kojima et al., 2009). They obtained 3.81% and 3.13% power conversion efficiency (PCE), respectively, using $CH_3NH_3PbI_3$ and $CH_3NH_3PbBr_3$ as photovoltaic cell visible-light sensitizers. Numerous research has already been done on the advancement of perovskite solar cells. Previously, Hagfeldt and colleagues had achieved a maximum efficiency of 20.8% (Xu et al., 2017). The most significant skyrocketed power conversion efficiency of organic-inorganic hybrid perovskite reported to date is 26.1% (NREL report 2022). It has been exemplified by the certified power conversion efficiencies achieved by them so far. According to theory, in organic-inorganic hybrid perovskites, the effective mass, intrinsic mobility, recombination lifetime, and diffusion length of the two types of carriers is comparable which is responsible for their excellence in the photovoltaic field (Kumar and Babu, 2021; Liu et al., 2023). The main causes of this noteworthy progress are enhanced film deposition methods and device structural design. It is generally known that the presence of compact, homogeneous perovskite films with a significant amount of crystallization is essential for devices' stability, repeatability, and performance. On account of this, organic-inorganic hybrid halide materials can be used to provide better optical and photovoltaic performance to realize

* Corresponding authors.
E-mail addresses: vidya.891@gmail.com (V. C. C), cc.vishwanath@gmail.com (V. C. C).

https://doi.org/10.1016/j.hazadv.2023.100368
Received 19 July 2023; Received in revised form 29 August 2023; Accepted 29 August 2023
Available online 31 August 2023

commercial applications. In an ideal world, individual materials would be optimized using a variety of synthetic procedures known to create better crystals with the necessary microstructure (Manukyan et al., 2016; Hao et al., 2014; Serrano-Lujan et al., 2015).

The structure of perovskite crystals is frequently described using the phrase "tolerance factor" (Balachandran et al., 2021). Despite substantial studies into such basic concepts, this is obvious that such a process of forming perovskite crystals in good correlation with Goldschmidt tolerance factor poses several distinct obstacles for investigators. However, as this property is essential for the construction of solar cell devices, a technique is still necessary to synthesize perovskites on the nano and microscale level with high homogeneity. With a conversion efficiency of more than 15%, on-chip perovskite solar cells have a lot of potential as innovative, large-scale, competitive photovoltaic devices (Vidyasagar et al., 2018; Li et al., 2021). The outcomes display that the spectral properties are almost the same, indicating which photovoltaic operating mechanism is distinct and provide increased diffusion lengths (1 m). Most of the performance differences between the devices may be attributed to the recombination rates due to the carrier's conductivity of the devices being essentially the same. These findings offer a special way to improve the performance of perovskite solar cells (Ke et al., 2021; Liu et al., 2022).

Lead perovskite solar cells are well known for their excellent power conversion efficiencies. However, toxicity of lead which has substantial toxicological effects on human health increases environmental harm and water-soluble lead halide perovskites in water have several risk factors that affect chemical poisoning in the food and serves as a barrier to perovskite solar cells' large-scale production and marketing. It is crucial to develop Pb-free perovskite in order to increase the competitiveness of perovskite solar cells (Kumar and Babu, 2021). Researchers are striving to create better-stability, flexible materials using lead-free components (Cu^{2+}, Sn^{4+} and Sb^{3+}). In 2015, it was shown how to prepare two hybrid perovskites of cupric bromide, (p-F-$C_6H_5C_2H_4$—$NH_3)_2CuBr_4$ and $(CH_3(CH_2)_3NH_3)_2CuBr_4$, and how to make the first copper-based perovskites-based solar cells. The PCE of the solar cells prepared was 0.50% and 0.63%, respectively. These devices are known for their great air stability, resulting in less than a 5% reduction in performance after a day in air with 50% humidity and no encapsulation (Vidyasagar et al., 2018; Kadhim and zamil Manshad, 2019; Ma et al., 2016).

Additional work shows that Cl is necessary to increase crystallinity against copper reduction and stabilize the perovskite $MA_2CuCl_xBr_{4-x}$. The Cl/Br ratio modification can be used to alter the optical absorbance from visible to infrared. A better power conversion efficacy was achieved utilizing $MA_2CuCl_2Br_2$ as a sensitizer with a band gap of 1.90 eV, a 216 (Acm^{-2}) Jsc and, a 256 mV Voc. These results demonstrate the realization of copper perovskite solar cell devices. As shown, perovskite preparation is important for applications in solar cells since a little variation in radius may cause the optical absorbance of perovskite to increase or decrease. As a result, researchers are constantly looking for new substances and generating new methods to enhance the characteristics of perovskites so as to attain better efficiencies. Cu-based perovskites have been shown to have a two-dimensional structure, in contrast to the normal three-dimensional structure of lead-based perovskites; this variance is caused by smaller ionic radii of Cu^{2+} ion. This ion is more stable in the atmosphere than Sn^{2+}. Powders of $(CH_3NH_3)_2CuCl_4$ were created to replace environmentally benign Pb^{2+} as a light absorber on mesoporous metal oxides. Future research will concentrate on developing lead-free ($(CH_3NH_3)_2CuCl_4$ perovskites), highly effective, and eco-friendly synthetic organic inorganic hybrid halide perovskite materials because $CH_3NH_3SnCl_3$ is unstable in the ambient atmosphere (Noel et al., 2014; Hao et al., 2014; Li et al., 2015; Koh et al., 2015; Xu et al., 2015; Wang et al., 2016; Ramavenkateswari and Venkatachalam, 2016).

In the current study, we suggest a ultrasonic assisted method to synthesize and compare the fundamental characteristics of perovskites based on Cu, Pb and Sn for use in energy conversion devices (Bhooshan et al., 2016; Moyez and Roy, 2018). A promising alternative for lead halide perovskites for solar applications is reported. Additionally, a higher emphasis on lead-free perovskites is suggested.

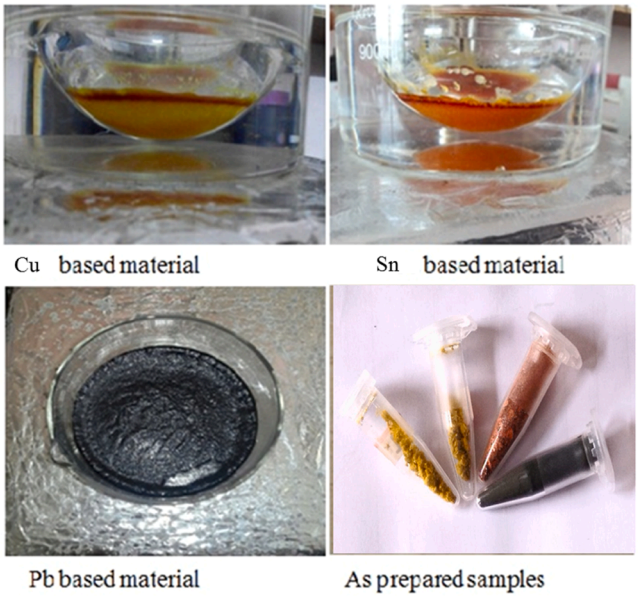

Fig. 1. As-prepared samples for solar cell applications in the laboratory.

2. Materials and methods

Methylamine 40% (CH_3NH_2), Copper chloride ($CuCl_2$ $2H_2O$), N, N-Dimethyl formamide and Lead chloride acquired from S D fine-chem. Limited (Mumbai, India). Tin chloride and HCl (55–58%) were procured from Merck. We have used analytical grade chemicals throughout the experiments.

2.1. Synthesis

In a typical synthesis, a 250 mL round bottom flask was filled with a combination of 28 mL of methylamine (CH_3NH_2) and 15 mL of hydrochloric acid (HCl), it was then cooled in an ice bath to avoid the formation of thick vapors caused by the dropwise addition of HCl. The reaction mixture was then kept at 0 °C and agitated for almost 2 h at 500 rpm. The reaction mixture was added to the petri dish, which was then sited in an oven fixed to 70 °C for around 4 h. Methyl ammonium chloride appears as a white crystal in the final product. The double-necked 100 mL RB flask is used to transfer this CH_3NH_3Cl product. In a further experiment, to ensure that $PbCl_2$ had completely dissolved, a standard solution of 0.3 M $PbCl_2$ in N, N-dimethyl formamide was prepared and stirred continuously for 2 h at 80 °C. After complete dissolution, the prepared 0.3 M $PbCl_2$ solution was loaded up in the burette and drop-wisely added to methyl ammonium chloride (CH_3NH_3Cl) in DMF that was kept in an RB flask by sonicating at 60 °C. The color of the mixture varied from pale yellowish to dark brown (yellow when adding $CuCl_2$, orange when adding $SnCl_2$) as the addition of $PbCl_2$ increased. The reaction specimens were placed onto the petri dish, and it was heated to 80 °C to evaporate the N, N-dimethyl formamide. The crystals were centrifuged to obtain solid, which is annealed at 70 °C. The final product of lead perovskites material is obtained after complete drying. Cu and Sn-based perovskites ($SnCl_2$ or $CuCl_2$ $6H_2O$) have been synthesized using a similar process (Fig. 1). The reaction mechanism proposed for $CH_3NH_3PbCl_3$ formation is

$$3CH_3NH_3Cl + PbCl_2 \rightarrow CH_3NH_3PbCl_3 + 2CH_3NH_3Cl\uparrow$$

When the sample is annealed at 80 °C, the CH_3NH_3Cl by-product,

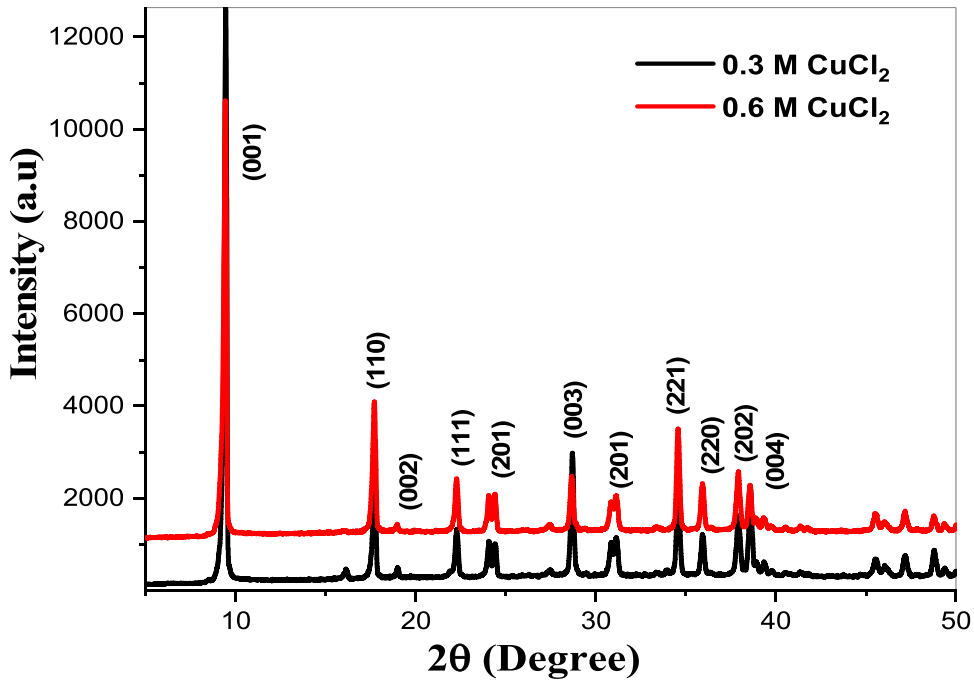

Fig. 2. Displays the XRD pattern of the $(CH_3NH_3)_2CuCl_4$ with different concentrations of Cu.

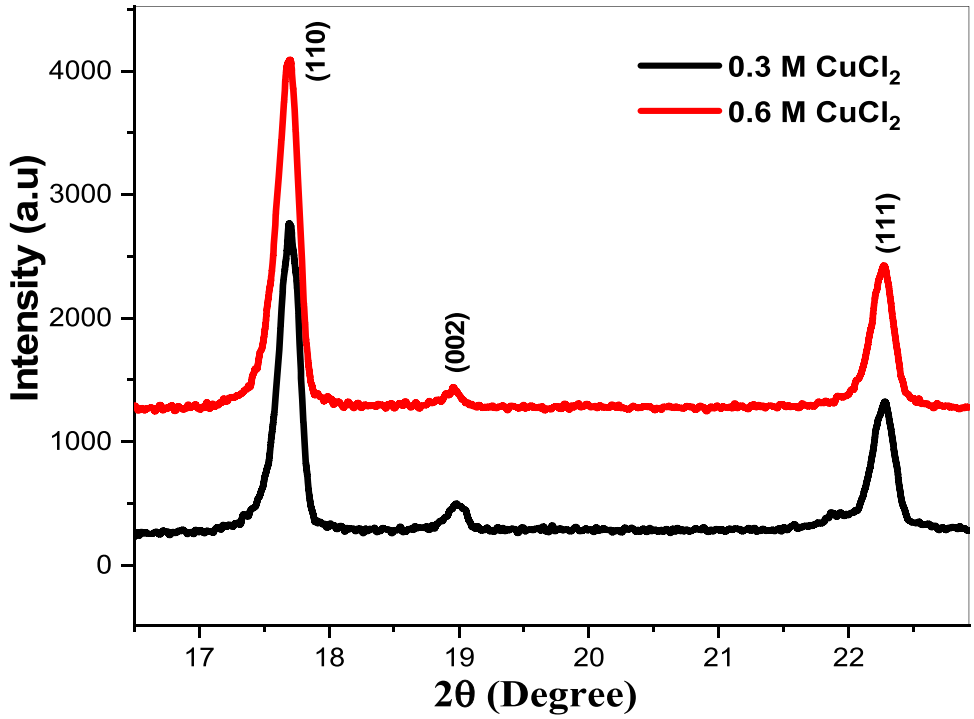

Fig. 3. Displays an inset view of the XRD pattern peaks (110), (002) and (111) of $(CH_3NH_3)_2CuCl_4$ material.

which is unstable, can readily escape from the sample.

3. Results and discussions

3.1. XRD analysis

To confirm that the reaction proceeds by the above-mentioned equation, a better understanding of the structure of the final products is required. As aforementioned, a liquid of N, N-dimethyl formamide was used to dissolve the CH_3NH_3Cl and $CuCl_2$. The production of Cu-based perovskites was observed using the X-ray diffraction (XRD) technique. All of the peaks with matching phases at 9.36°, 17.62°, 19.05°, 22.28°, 24.47°, 28.65°, 31.13°, 34.65°, 35.88° and 38.54° are attributed to the diffraction planes (001), (110), (002), (111), (201), (003), (221), (220), (202) and (004) which is in good agreement with the literature (Cortecchia et al., 2016). The XRD pattern showed no unreacted precursor or CuO peaks, which confirmed the samples' purity as prepared. The XRD patterns of $(CH_3NH_3)_2CuCl_4$ at different Cu

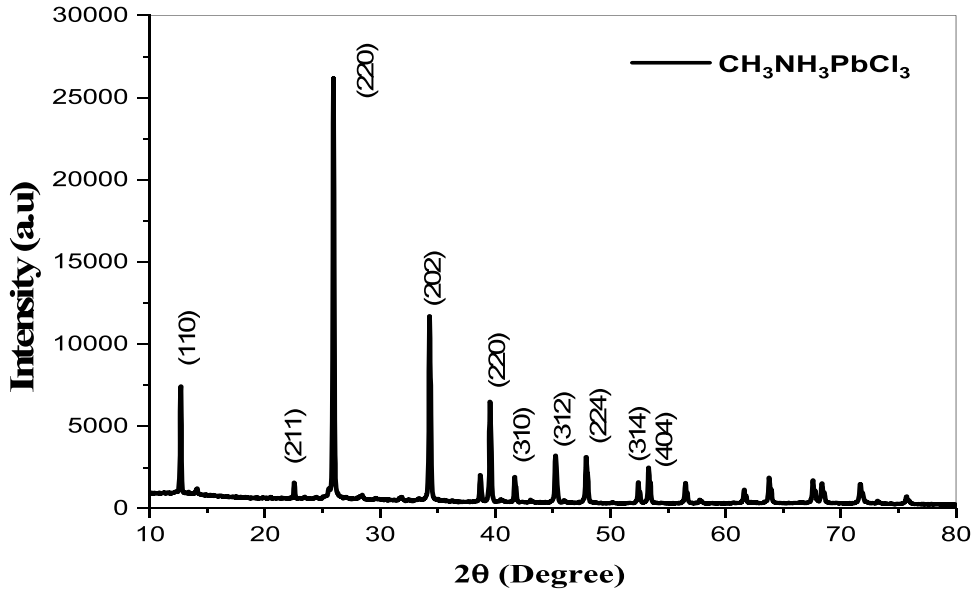

Fig. 4. Displays the XRD pattern of the $CH_3NH_3PbCl_3$ material.

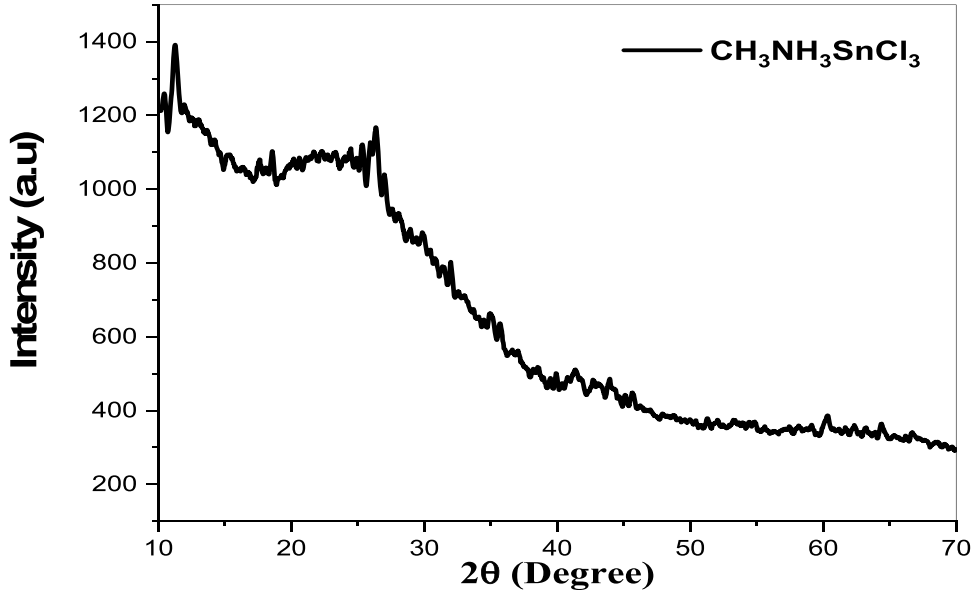

Fig. 5. Shows the XRD pattern of the $CH_3NH_3SnCl_3$ material.

concentrations are revealed in Figs. 2 and 3. It is determined that no doped Cu ions exist in CuO or other species since Cu-doped samples do not exhibit unique peaks (Fig. 2). Although $(CH_3NH_3)_2CuCl_4$'s XRD pattern is unaltered, the peak positions have been somewhat altered about 0.3 M Cu concentration, moving to the right slightly (at a higher angle). This shifting of the peak reveals the incorporation of Cu into the $(CH_3NH_3)_2CuCl_4$ lattice (Fig. 3). Peak intensities for all of the doped samples slightly dropped as the Cu content enhanced; which could be due to the crystal structure is unaffected by Cu doping, which alters only the crystallinity. The production of a sTable 3-dimensional crystal structure of perovskite is often indicated by values for t and r from Goldschmidt tolerance factor, so for copper perovskite it suggests that perovskite has been crystallized in a lower dimension that is 2-D (Balachandran et al., 2021).

It demonstrates that the lattice parameter has drastically altered. This means that Cl is present at specified points within the perovskite crystal. While a 3:1 ratio is ideal for Cl doping, reaction/fabrication factors can change the actual concentration in the final product. The color quickly shifted from yellow to dark brown as the two precursors were combined. The peaks at 12.60°, 22.60°, 25.10°, 34.50°, 39.55°, 42.01°, 45.20°, and 47.85° are all assigned to the diffraction planes (110), (211), (220), (202), (310), (312), and (224), respectively, as revealed in Fig. 4.

The purity of the samples is confirmed by the disappearance of unreacted precursor or PbO_2 peaks in the XRD pattern. No more peaks for PbO_2 were found, and the non-reacted $PbCl_2$ is responsible for a minor peak of around 2θ=13.6 ° (shown by arrows). The Sn-based perovskite materials' powder XRD pattern is shown in Fig. 5. The synthesized $CH_3NH_3SnCl_3$ has a perovskite structure, as shown by the diffraction peaks of 2θ, which are 11.2°, 27.1°, and 58.1° The (001) and (312) planes on the $SnCl_2$ PDF card correspond to the peaks of 2θ 11.2° and 58.1°, respectively, showing that SnO_2 may not be present. The investigational X-ray diffraction patterns of $CH_3NH_3SnCl_3$ are shown in Fig. 5. When exposed to air, the undesired $SnCl_2$ hydrates, but when

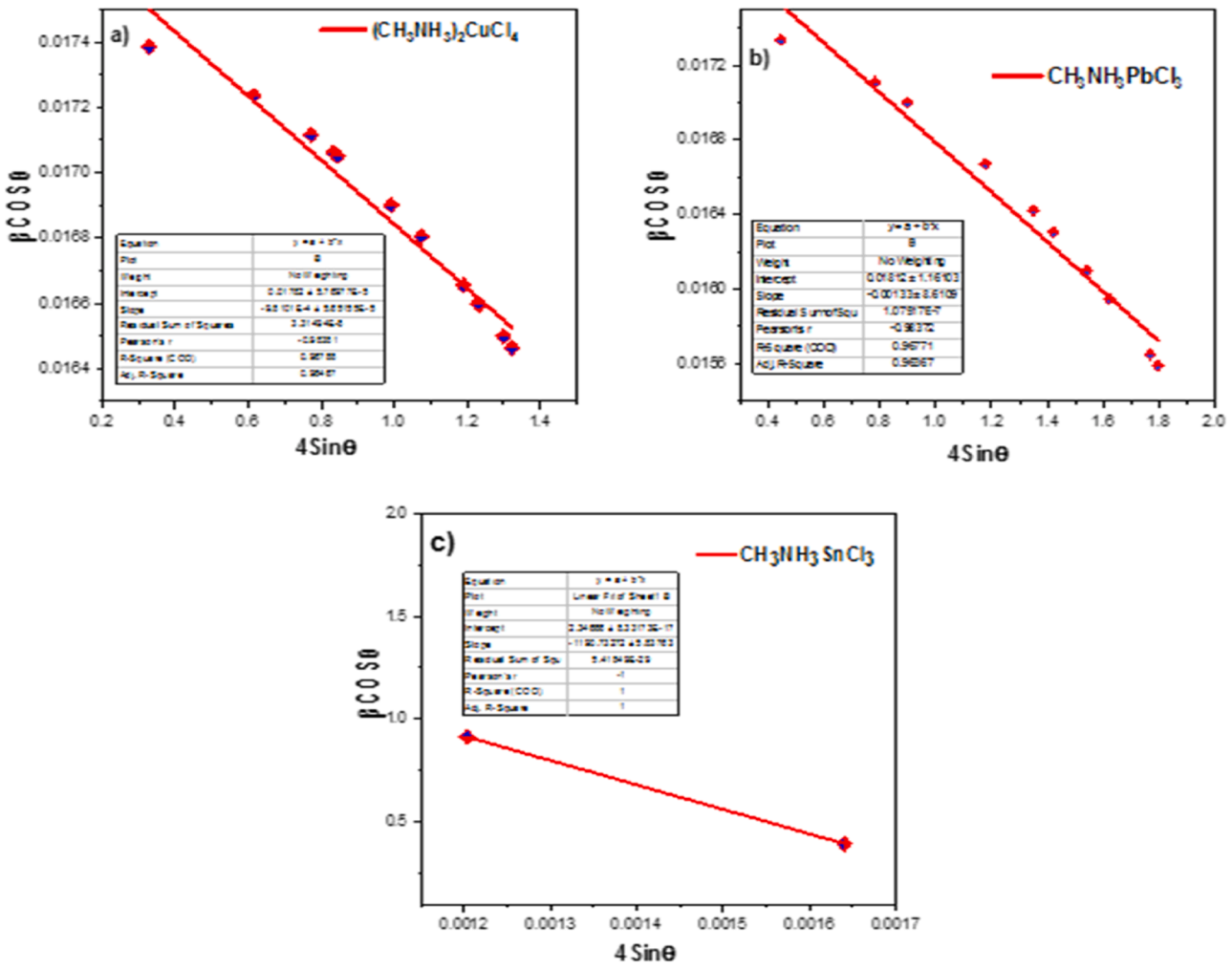

Fig. 6. The W-H analysis of $(CH_3NH_3)_2CuCl_4$, $CH_3NH_3PbCl_3$, and $CH_3NH_3SnCl_3$ crystals. The strain is calculated from the fit's slope, while the crystalline size is calculated from the fit's y-intercept.

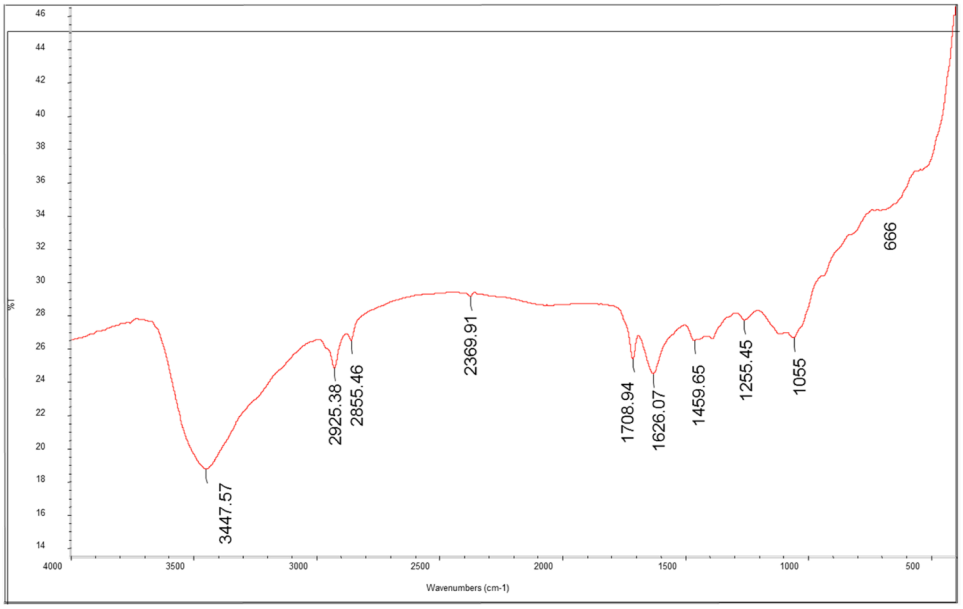

Fig. 7. Shows the FTIR spectra of the $(CH_3NH_3)_2CuCl_4$ material.

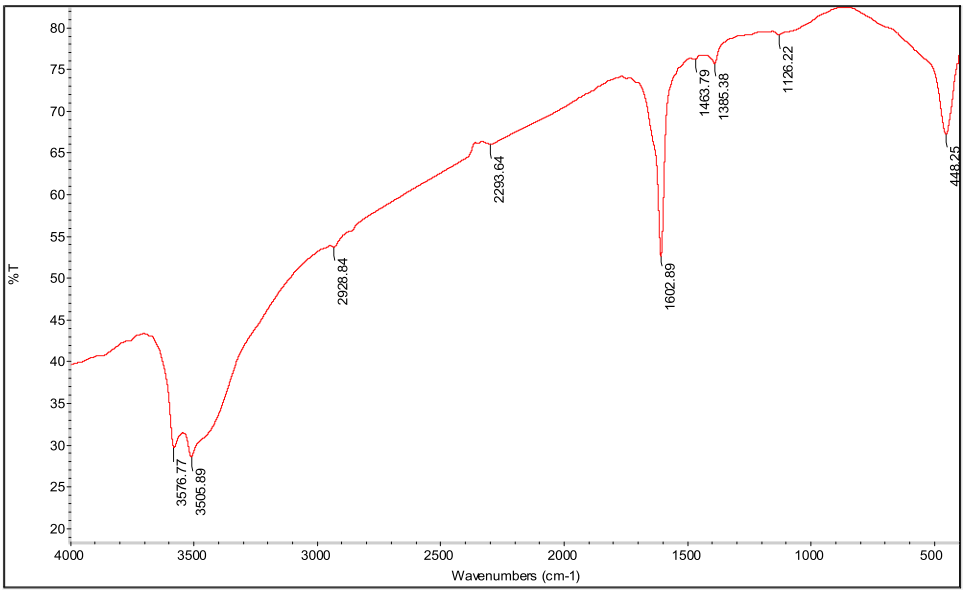

Fig. 8. Shows the FTIR spectra of the $CH_3NH_3PbCl_3$ material.

exposed to oxygen, the unstable Sn rapidly oxidizes. Insufficient nucleation avoids the formation of the required perovskite amorphous phase.

For the crystals $(CH_3NH_3)_2CuCl_4$, $CH_3NH_3PbCl_3$, and $CH_3NH_3SnCl_3$, we also calculated the lattice strain. Using the William-Hall Method, the strain is calculated from the fit's slope, and crystallite size is calculated from the fit's y-intercept. However, when utilizing the William-Hall method, the sizes of the crystallites for $(CH_3NH_3)_2CuCl_4$ are frequently larger than those for $CH_3NH_3PbCl_3$ and $CH_3NH_3SnCl_3$ crystals. The difference in crystallite size between Scherrer's equation and William-Hall is negligible since Scherrer's equation employs the greatest intense peak whereas William-Hall employs an average of several peaks. This demonstrated that the micro-strain is inversely related to the size of the crystals (Fig. 6).

3.2. FTIR analysis

FT-IR spectroscopy was used to analyze each sample. The stretching vibration of N—H is shown in Fig. 7 by a distinct band at around 3447 cm^{-1}. It is known that the bands in sample at 2925 cm^{-1} are C—H stretching bands. This C—H stretching vibration is related to the CH_3^+ group of the organic cation. The band at 1626 cm^{-1} is obtained by the bending vibrations of N—H with symmetry and asymmetry. At 1459 cm^{-1}, the C—H bond's symmetry and asymmetry vibrations are seen. The stretching vibrations of the C—N bands may be detected at 1255 cm^{-1} in the spectra. Strong alkyl halides have a C—Cl stretch, which is shown by the slight hump at 666 cm^{-1}. Thus, the $(CH_3NH_3)_2CuCl_4$ samples are analyzed using FTIR to confirm the existence of all functional groups.

According to Fig. 8, the stretching vibration of N—H is represented

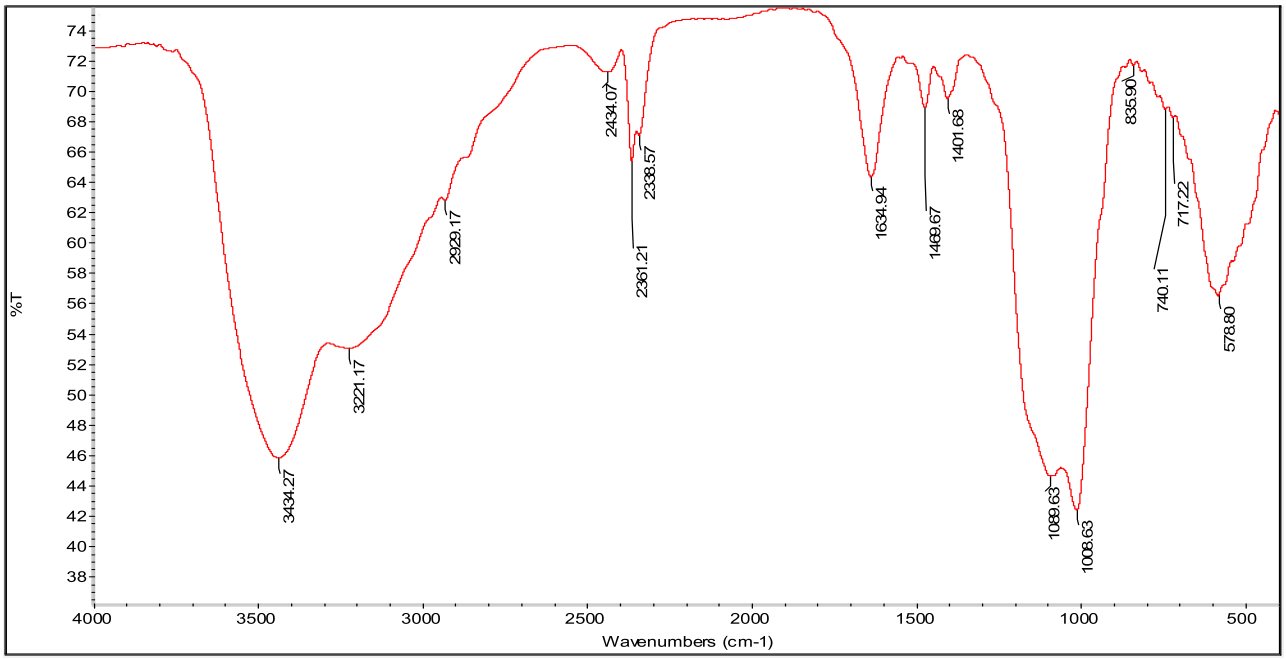

Fig. 9. Displays the FTIR spectra of the $CH_3NH_3SnCl_3$ material.

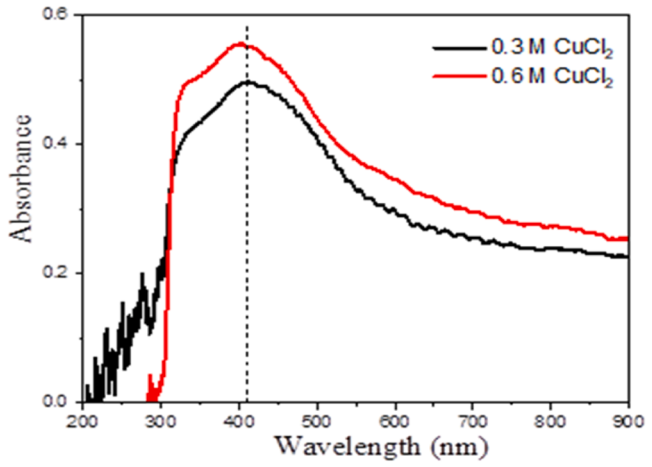

Fig. 10. Shows the UV–Visible spectra of $(CH_3NH_3)_2CuCl_4$ at different Cu concentrations.

by a distinct small hump at 3447 cm^{-1}. Additionally, the main peak positions between 3578 and 3505 cm^{-1} are connected to N—H stretch vibrations, which may be related to the NH_3^+ group of the organic cation. The sample included the C—H stretching bands at a range of 2928 cm^{-1}. This stretching vibration of C—H is related to the CH_3^+ group of the organic cation. The band at 1602 cm^{-1} is obtained by the bending vibrations of N—H with symmetry and asymmetry. The bond vibrations of C—H are shown to have both symmetry and asymmetries at 1463 cm^{-1}. The spectra show stretched C—N vibration bands at 1126 cm^{-1}. The C—Cl stretch is represented by the slight hump at 448 cm^{-1}, which is associated with strong alkyl halides. As a consequence, the FTIR data demonstrate that all functional groups are present in the $CH_3NH_3PbCl_3$ samples.

According to Fig. 9, a distinct band at 3434 cm^{-1} represents the N—H stretching vibration. The stretching vibrations of N—H, which might be connected to the NH_3^+ group of the organic cation, are also linked to the significant peak positions between 3434 and 3221 cm^{-1}. At 2929 cm^{-1}, C—H stretching bands were found. The CH_3^+ group of the organic cation is coupled to this stretching vibration of C—H. The band is formed at 1634 cm^{-1} by the symmetry and asymmetry bending vibrations of N—H. At 1469 cm^{-1}, the symmetry and asymmetry of the C—H bond vibrations are displayed. The spectra at 1008 cm^{-1} exhibit stretching C—N vibration bands. The little hump is associated with strong alkyl halides and corresponds to the C—Cl stretch at 578 cm^{-1}. As a consequence, the FTIR analysis reveals that the $CH_3NH_3SnCl_3$ samples contain all functional groups.

3.3. Optical properties

As seen in Fig. 10, UV–Visible spectroscopy is a useful non-destructive method for calculating the band gap energy of perovskites. To study the optical properties of charge carriers produced by photons, metal-organic halide perovskites were used. Methylammonium cations occupy the gaps left by the metal halide octahedra in the structure of

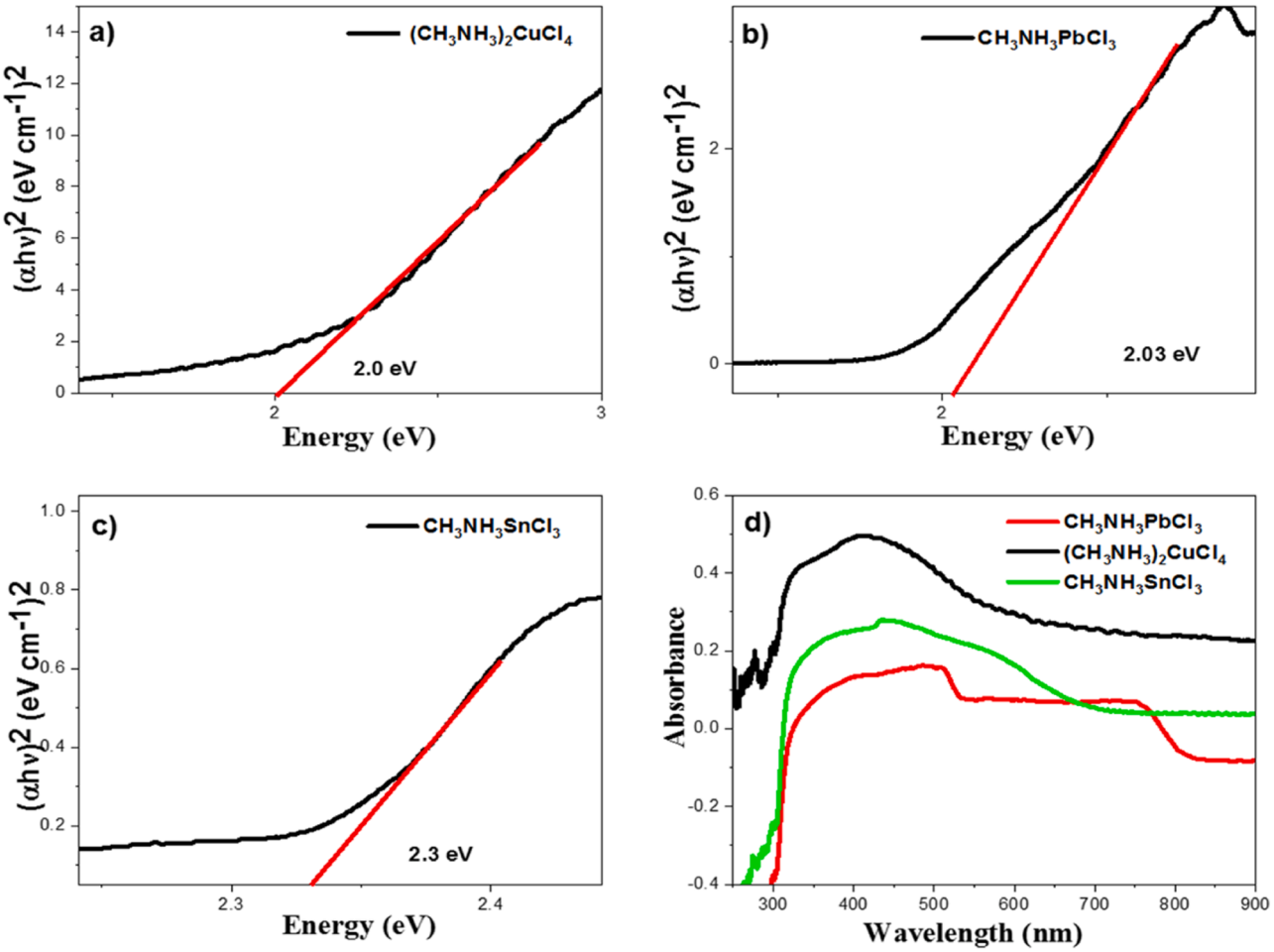

Fig. 11. Tauc's plot of $(CH_3NH_3)_2CuCl_4$ (a), $CH_3NH_3PbCl_3$ (b), $CH_3NH_3SnCl_3$ (c) and UV–Visible spectra of $(CH_3NH_3)_2CuCl_4$, $CH_3NH_3PbCl_3$ and $CH_3NH_3SnCl_3$ crystals (d).

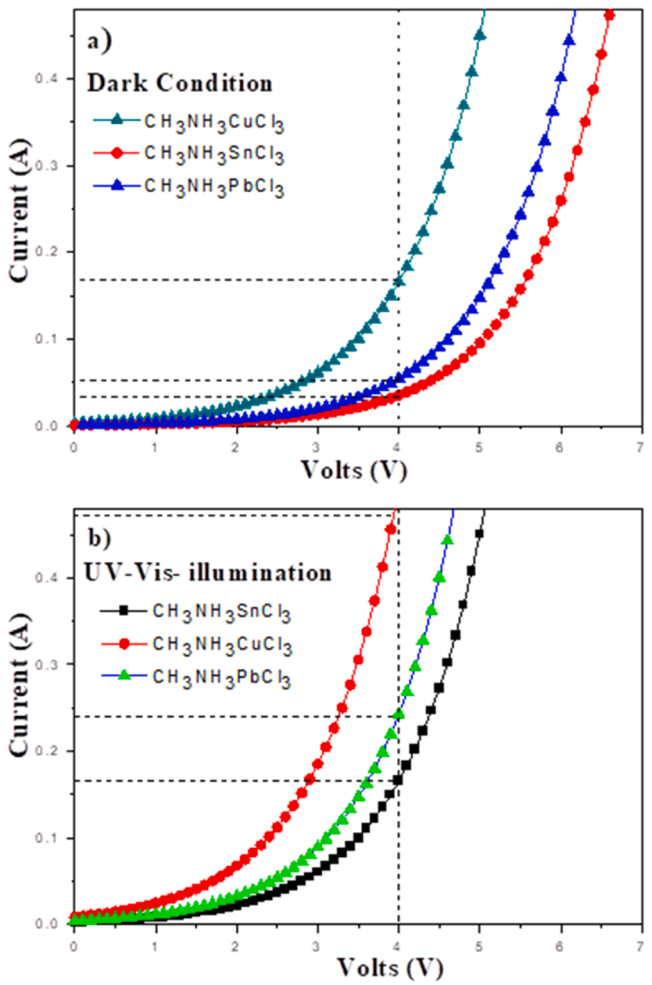

Fig. 12. *I-V* characteristic curves of $(CH_3NH_3)_2CuCl_4$, $CH_3NH_3PbCl_3$, and $CH_3NH_3SnCl_3$ at dark conditions (a), and UV–Visible illumination (b).

organic-inorganic halide perovskite, which are made up of a framework of corner-sharing octahedra. The excitonic absorption peaks of the metal-organic halide perovskite could be turned into a variety of absorption spectra, and when metal atoms and halogens changed, the absorption spectrum in visible light changed significantly. For instance, the band gap in $CH_3NH_3PbCl_3$ (ABX_3) varied from 2.03 to 2.0 and 2.03 to 2.3 eV, respectively, when Cu and Sn are replaced for the B sites. The recombination of lower energy hole-electron pairs is thought to be the cause of the band gap narrowing when secondary energy levels are added between both the valence band and conduction bands. The analysis found that the interaction between the inorganic matrix and MA^+has an impact on the electronic structure of $(CH_3NH_3)_2CuCl_4$, $CH_3NH_3PbCl_3$, and $CH_3NH_3SnCl_3$. It suggests that the band is significantly influenced by both the MA^+distribution and the phases. Furthermore, compared to $(CH_3NH_3)_2CuCl_4$ and $CH_3NH_3PbCl_3$, $CH_3NH_3SnCl_3$ has a wider band gap. The perovskite samples absorb in the red at and above 700 nm, it is the desired property in optoelectronic and energy appliances. This demonstrates that the range of light that halide perovskite can absorb in wider than the visible spectrum. According to Tauc's relation, the following equation relates the optical band gap energy that exists inside the bands of any material, absorbing incident photon energy *(hν)* and the absorption coefficient *(α)* (Yathisha et al., 2016).

$$Ah\nu = A\left(h\nu - E_g\right)^n \tag{1}$$

Where *n* is an index, *ν* is photon frequency, and *A* is a constant. Both the direct and indirect transitions have $n = ½$ and *2*, respectively. The semiconductor ABX_3 has a straight band gap in this instance. The band gap was determined by Tauc's plot Fig. 11.

3.4. Electrical properties

Cu, Pb, and Sn-based perovskite pellet's current-voltage (I-V) properties were studied while making excellent electrical contact with a silver paste. Fig. 12 displays the *I-V* characteristics of perovskites made of Cu, Pb, and Sn. When analyzing the electrical properties of perovskites made using a simple solvent-based method, resistance, and current intensity are two crucial variables. It proves that all prepared perovskites have non-linear characteristics in both light and dark environments. In the dark, the lead-based perovskite's current intensity was equivalent to that of the perovskites made of Cu and Sn (Fig. 12**a**).

The bandgap of a material has a significant impact on the power conversion efficiency (Raj et al., 2023). It determines the energy of photons from sunlight that the material can absorb. Excitons are formed in the material when photons with energies greater than the bandgap energy are absorbed. When these electron-hole pairs are separated and gathered at the device's contacts, they can then help in the creation of electrical current. It may ineffectively absorb low-energy photons if the bandgap is too small. It might miss out on a sizable chunk of the solar spectrum if the bandgap is too high. Achieving high power conversion efficiency in solar cells requires optimizing the bandgap for the sun spectrum.

The electron moves from the valence band to the conduction band more quickly with a narrower band gap, which results in a higher current intensity. The *I-V* properties of Cu, Pb, and Sn-based perovskites are displayed in Fig. 12**b** when they are subjected to UV–visible radiation. It reveals that upon exposure to UV-visible radiation, all samples of Cu, Pb, and Sn-based perovskites show a considerable rise in the current range (curves shift to the less potential side). This demonstrates that as UV-visible light is absorbed, electrons from organic cation molecules in the crystal interact and produce electron-hole pairs. On the contrary hand, the remaining electrons in the conduction band carry a greater intensity of the current. **Figs. 11 and 12** display the band gap energy and current range results (in both light and dark conditions). The intrinsic defectiveness in Cu, take the role of Pb and make the conductivity of electricity better. Additional carrier electrons are drawn into the conduction band when Cu and Sn replace Pb. The $(CH_3NH_3)_2CuCl_4$ perovskite that was synthesized proves that UV–Visible light absorption generates more electron-hole pairs than $CH_3NH_3PbCl_3$ and $CH_3NH_3SnCl_3$ do by significantly increasing conductivity under UV–Visible light conditions (Fig. 12**b**).

4. Conclusion

In summary, this research showed the alternative option that have evolved over the years to replace hazardous metals like Pb and Sn due to the possible adverse impact on both people and the environment. The methyl ammonium chloride and appropriate amounts of $CuCl_2$, $PbCl_2$, and $SnCl_2$ were dissolved in DMF using sonication to produce the $(CH_3NH_3)_2CuCl_4$, $CH_3NH_3PbCl_3$, and $CH_3NH_3SnCl_3$ perovskites respectively. The peak intensities of all the samples were verified by the XRD data to be sharp, including a narrow FWHM, as well as being in a highly crystalline form at their initial state of production. The two different concentrated Cu-based perovskite samples had identical crystal structures when compared to one another, however, we observed a slight variation in the XRD peaks. According to Tauc's plot, which compares $CH_3NH_3PbCl_3$ with $CH_3NH_3SnCl_3$, the optical band gap of $(CH_3NH_3)_2CuCl_4$ is significantly smaller. The *I-V* characteristic measurements demonstrate that $(CH_3NH_3)_2CuCl_4$ exhibits a more photosensitive behavior than $CH_3NH_3PbCl_3$, and $CH_3NH_3SnCl_3$. Our findings provide information on electrical and optical characteristics. The findings also present a new method for examining the perovskite material's

constrained optical characteristics. Before constructing a photovoltaic device, material optimization that results in optical improvement is essential. Therefore, hybrid halide perovskite, from our perspective, will dominate photovoltaic and optoelectronic applications.

Declaration of Competing Interest

The authors declare that they have no known competing financial interests or personal relationships that could have appeared to influence the work reported in this paper.

Data availability

No data was used for the research described in the article.

Acknowledgments

The authors are grateful to Rani Channamma University, Belgaum and IISc, Bangalore for characterization of samples for laboratory facilities, the authors are also thanking Science and Engineering Research Board, Department of Science and Technology Govt. of India and Vision group on Science and Technology, Govt. of Karnataka for the financial assistance in terms of project grants. One of the authors, Swapna S. Chigari is grateful to UGC—CSIR, New Delhi for financial support in the form of Junior research fellowship.

References

Balachandran, N., Robert, T.M., Jayalatha, T., Neema, P.M., Mathew, D., Cyriac, J., 2021. optical properties. J Alloys Compd 879, 160325. https://doi.org/10.1016/j.jallcom.2021.160325.

Bhooshan, V., Gouda, L., Gedanken, A., 2016. Ultrasonics Sonochemistry Sonochemical synthesis of $CH_3NH_3PbI_3$ perovskite ultrafine nanocrystal sensitizers for solar energy applications. Ultrason. Sonochem 32, 54–59. https://doi.org/10.1016/j.ultsonch.2016.02.012.

Cortecchia, D., Dewi, H.A., Yin, J., Bruno, A., Chen, S., Baikie, T., Boix, P.P., Grätzel, M., Mhaisalkar, S., Soci, C., Mathews, N., 2016. Lead-Free $MA_2CuCl_xBr_{4-x}$ Hybrid Perovskites. Inorg. Chem 55, 1044–1052. https://doi.org/10.1021/acs.inorgchem.5b01896.

Dey, A., Ye, J., De, A., Debroye, E., Ha, S.K., Bladt, E., Kshirsagar, A.S., Wang, Z., Yin, J., Wang, Y., Quan, L.N., Yan, F., Gao, M., Li, X., Shamsi, J., Debnath, T., Cao, M., Scheel, M.A., Kumar, S., Steele, J.A., Gerhard, M., Chouhan, L., Xu, K., Wu, X., Li, Y., Zhang, Y., Dutta, A., Han, C., Vincon, I., Rogach, A.L., Nag, A., Samanta, A., Korgel, B.A., Shih, C., Gamelin, D.R., Son, D.H., Zeng, H., Zhong, H., Sun, H., Demir, H.V., Scheblykin, I.G., Stolarczyk, J.K., Zhang, J.Z., Feldmann, J., Hofkens, J., Luther, J.M., Julia, P., Li, L., Manna, L., Bodnarchuk, M.I., Kovalenko, M.V., Roe, M.B.J., Pradhan, N., Mohammed, O.F., Bakr, O.M., Yang, P., Mu, P., Kamat, P.V., Bao, Q., Zhang, Q., Krahne, R., Galian, R.E., Stranks, S.D., Bals, S., Biju, V., Tisdale, W.A., Yan, Y., Hoye, R.L.Z., Polavarapu, L., 2021. State of the art and prospects for Halide Perovskite Nanocrystals. ACS Nano 15, 10775–10981. https://doi.org/10.1021/acsnano.0c08903.

Haug, F., Yum, J., Ballif, C., 2014. Organometallic Halide Perovskites: sharp optical absorption edge and its relation to Photovoltaic Performance. J Phys Chem Lett 5, 1035–1039. https://doi.org/10.1021/jz500279b.

Hao, F., Stoumpos, C.C., Cao, D.H., Chang, R.P.H., Kanatzidis, M.G., 2014. Lead-free solid-state organic-inorganic halide perovskite solar cells. Nat Photonics 8, 489–494. https://doi.org/10.1038/nphoton.2014.82.

Kadhim, B.B., zamil Manshad, A., 2019. Optical properties of perovskite thin film. Al-Mustansiriyah J. Sci. 30, 174–177. https://doi.org/10.23851/mjs.v30i1.564.

Koh, T.M., Krishnamoorthy, T., Yantara, N., Shi, C., Leong, W.L., Boix, P.P., Grimsdale, A.C., Mhaisalkar, S.G., Mathews, N., 2015. Formamidinium tin-based perovskite with low E_g for photovoltaic applications. J. Mater. Chem. A 3, 14996–15000. https://doi.org/10.1039/c5ta00190k.

Kojima, A., Teshima, K., Shirai, Y., Miyasaka, T., 2009. Organometal halide perovskites as visible-light sensitizers for photovoltaic cells. J. Am. Chem. Soc 131, 6050–6051. https://doi.org/10.1021/ja809598r.

Kumavat, S.R., Sonvane, Y., Singh, D., Gupta, S.K., 2019. Two-dimensional $CH_3NH_3PbI_3$ with high efficiency and superior carrier mobility: a theoretical study. J. Phys. Chem. C 123, 5231–5239. https://doi.org/10.1021/acs.jpcc.8b11427.

Kumar, N.S., Babu, K.C., 2021. A review on perovskite solar cells (PSCs), materials and applications. J. Materiom. 7, 940–956. https://doi.org/10.1016/j.jmat.2021.04.002.

Li, X., Zhang, J., Huo, Y., Dai, K., Li, S., Chen, S., 2021a. Applied catalysis B: environmental heterostructures nanocomposite with e ff ective interfacial charge transfer and mechanism insight. Environmental 280, 119452. https://doi.org/10.1016/j.apcatb.2020.119452.

Liu, L., Wang, Z., Zhang, J., Ruzimuradov, O., Dai, K., Low, J., 2023. Tunable interfacial charge transfer in a 2D–2D composite for efficient visible-light-driven CO_2 conversion. Adv. Mater. 25, 2300643 https://doi.org/10.1002/adma.202300643.

Li, X., Zhang, J., Huo, Y., Dai, K., Li, S., Chen, S., 2021b. Two-dimensional sulfur- and chlorine-codoped g-C_3N_4/CdSe-amine heterostructures nanocomposite with effective interfacial charge transfer and mechanism insight. Appl. Catal. B 280, 119452. https://doi.org/10.1016/J.APCATB.2020.119452.

X. Ke, J. Zhang, K. Dai, K. Fan, C. Liang, Integrated S-scheme heterojunction of amine-functionalized 1D CdSe nanorods anchoring on ultrathin 2D SnNb2O6 nanosheets for robust solar-driven CO2 conversion, 2000805 (2021) 1–11. doi:10.1002/solr.202000805.

L. Liu, A. Najar, K. Wang, M. Du, S.F. Liu, Perovskite quantum dots in solar cells, 2104577 (2022) 1–20. doi:10.1002/advs.202104577.

Li, Y., Yan, W., Li, Y., Wang, S., Wang, W., Bian, Z., Xiao, L., Gong, Q., 2015. Direct Observation of Long Electron-Hole Diffusion Distance in $CH_3NH_3PbI_3$ Perovskite Thin Film. Sci Rep 5, 14485. https://doi.org/10.1038/srep14485.

Manukyan, K.V., Yeghishyan, A.V., Moskovskikh, D.O., Kapaldo, J., Mintairov, A., Mukasyan, A.S., 2016. Mechanochemical synthesis of methylammonium lead iodide perovskite. J Mater Sci 51, 9123–9130. https://doi.org/10.1007/s10853-016-0165-4.

L. Ma, F. Hao, C.C. Stoumpos, B.T. Phelan, M.R. Wasielewski, M.G. Kanatzidis, Carrier Di ff usion lengths of over 500 nm in lead-free perovskite, 138 (2016) 6–11. doi:10.1021/jacs.6b09257.

Moyez, S.A., Roy, S., 2018. Thermal engineering of lead-free nanostructured $CH_3NH_3SnCl_3$ perovskite material for thin-film solar cell. J. Nanopart. Res. 20, 5. https://doi.org/10.1007/s11051-017-4108-z.

Noel, N.K., Stranks, S.D., Abate, A., Wehrenfennig, C., Guarnera, S., Haghighirad, A.A., Sadhanala, A., Eperon, G.E., Pathak, S.K., Johnston, M.B., Petrozza, A., Herz, L.M., Snaith, H.J., 2014. Lead-free organic-inorganic tin halide perovskites for photovoltaic applications. Energy Environ. Sci 7, 3061–3068. https://doi.org/10.1039/c4ee01076k.

NREL report 2022 “https://www.nrel.gov/pv/cell-efficiency.html”.

Ramavenkateswari, K., Venkatachalam, P., 2016. Stable tin chloride perovskite sensitized silver doped titania nanosticks photoanode solar cells with different hole transport materials. J. Inorg. Organomet. Polym. Mater 26, 981–990. https://doi.org/10.1007/s10904-016-0410-y.

Raj, A., Kumar, M., Kumar, A., Singh, K., Sharma, S., Singh, R.C., Pawar, M.S., Yahya, M. Z.A., Anshul, A., 2023. Comparative analysis of ‘La’ modified $BiFeO_3$-based perovskite solar cell devices for high conversion efficiency. Ceram. Int 49, 1317–1327. https://doi.org/10.1016/J.CERAMINT.2022.09.112.

Vidyasagar, C.C., Muñoz Flores, B.M., Jiménez Pérez, V.M., 2018a. Recent advances in synthesis and properties of hybrid Halide Perovskites for Photovoltaics. Nano-Micro Lett 10, 8. https://doi.org/10.1007/s40820-018-0221-5.

Xu, B., Zhang, J., Hagfeldt, A., Jen, K., Sun, L., Xu, B., Zhang, J., Hua, Y., Liu, P., Wang, L., Ruan, C., Li, Y., Tailor-making low-cost Spiro[fluorene-9,9′-xanthene]-based 3D Oligomers for Perovskite solar cells tailor-making low-cost 3D Oligomers for Perovskite solar cells, 54 (2017) 676–687. doi:10.1016/j.chempr.2017.03.011.

Serrano-Lujan, L., Espinosa, N., Larsen-Olsen, T.T., Abad, J., Urbina, A., Krebs, F.C., 2015. Tin- and lead-based perovskite solar cells under scrutiny: an environmental perspective. Adv Energy Mater 5, 1–5. https://doi.org/10.1002/aenm.201501119.

Vidyasagar, C.C., Hosamani, G., Kariyajjanavar, P., Yathisha, R.O., Nayaka, Y.Arthoba, 2018b. One-pot microwave synthesis and effect of Cu2+ ions on structural properties of Cu-ZnO Nano Crystals. Mater. Today: Proc. 5, 22171–22180. https://doi.org/10.1016/j.matpr.2018.06.582.

Xu, X., Chen, Q., Hong, Z., Zhou, H., Liu, Z., Chang, W.H., Sun, P., Chen, H., De Marco, N., Wang, M., Yang, Y., 2015. Working mechanism for flexible perovskite solar cells with simplified architecture. Nano Lett 15, 6514–6520. https://doi.org/10.1021/acs.nanolett.5b02126.

Wang, L.Z., Zhao, Y.Q., Liu, B., Wu, L.J., Cai, M.Q., 2016. First-principles study of photovoltaics and carrier mobility for non-toxic halide perovskite $CH_3NH_3SnCl_3$: theoretical prediction. Phys. Chem. Chem. Phys. 18, 22188–22195. https://doi.org/10.1039/c6cp03605h.

Yathisha, R.O., Nayaka, Y.A., Vidyasagar, C.C., 2016. Microwave combustion synthesis of hexagonal prism shaped ZnO nanoparticles and effect of Cr on structural, optical and electrical properties of ZnO nanoparticles. Mater. Chem. Phys 181, 167–175. https://doi.org/10.1016/j.matchemphys.2016.06.046.